

Field mapping with the magnetic resonance force microscope

Todd G. Ruskell, Markus Löhndorf, and John Moreland^{a)}

National Institute of Standards and Technology, Boulder, Colorado 80303

(Received 4 January 1999; accepted for publication 21 March 1999)

We have developed magnetic resonance force microscopy for quantitative measurements of magnetic fields. A microscopic particle attached near the end of a microcantilever serves as the field sensing probe. We have demonstrated two-dimensional field mapping with a lateral resolution of 3.2 μm and a field resolution of 0.19 mT (1.9 G). The instrument holds considerable promise for field mapping with spatial resolution better than 0.1 μm at room temperature. Applications include field mapping of magnetic recording heads. [S0021-8979(99)00513-7]

I. INTRODUCTION

In this article we describe a method for extending magnetic resonance field metrology to microscopic scales. The technique relies on the high sensitivity provided by the newly developed magnetic resonance force microscope (MRFM). Magnetic resonance phenomena are the basis for the most accurate measurements of magnetic fields. This is a direct result of the Larmor relationship for the resonant condition: $B = \omega/\gamma$. B is the static flux density at which magnetic spins with a gyromagnetic ratio of γ resonantly precess when subjected to a transverse rf field oscillating at an angular frequency ω . Typical magnetic resonance probes are relatively large and are thus only useful for measurements of fairly uniform fields generated by macroscopic magnets.

Magnetic resonance probe sensitivity has improved with the development of high resolution magnetic resonance imaging (MRI) instruments. MRI instruments establish a known field gradient that is required to spatially resolve an unknown distribution of magnetic spins in a sample. Higher resolution imaging naturally requires sensitivity to a smaller number of spins. The signal-to-noise ratio (SNR) is ultimately limited by the quality factor Q of the pick-up coil tank circuit. The spatial resolution of conventional MRI instruments can also be limited by the relatively low field gradients (on the order of 0.1 T/m) that can be generated with wire-wound coils.

MRFM was first proposed by Sidles in 1991 as a way to overcome the limitations of conventional MRI microscopy with inductive coil probes.¹ Rugar *et al.* subsequently demonstrated the first magnetic resonance force microscope with electron spin resonance (ESR).² MRFM has also been demonstrated with nuclear magnetic resonance (NMR) by Züger *et al.*³ and Schaff *et al.*⁴ and with ferromagnetic resonance (FMR) by Zhang *et al.*⁵ MRFM instrumentation has benefited from the development of ultrasensitive cantilevers,⁶ optimal control of cantilever vibration,⁷ and operation at low temperatures.^{8,9}

So far, MRFM has been mainly applied to spatially resolving the spin density of a sample. However, the sensitivity

of MRFM also offers the possibility of reducing the size of the magnetic resonance field sensor for magnetic field calibration at submicrometer dimensions. Field strength can then be measured with a resolution limited by the resonant line shape and the spatial extent of the resonant probe. We report here a demonstration of high resolution field measurements using MRFM.

II. EXPERIMENTAL PRINCIPLES

We begin by considering a material which exhibits a strong ESR signal as a field sensor. The electron spin density of the field sensor is assumed to be uniform, and the spins are aligned in the same direction with a large external field. In this case, given a magnetic resonance field sensor of volume V mounted on a cantilever, the z component of the force between the field sensor and the field being measured is

$$F_z = VM_z \left(\frac{\partial B_z}{\partial z} \right). \quad (1)$$

Here \mathbf{M} is the magnetization of the sensor material and \mathbf{B} is a nonuniform flux density produced by some magnetic device. Equation (1) is valid under the condition of small lateral sensor magnetization such that $M_x \approx M_y \approx 0$. For a paramagnetic sensor in a transverse rf magnetic field of magnitude B_{rf} and angular frequency ω , M_z can be written as¹⁰

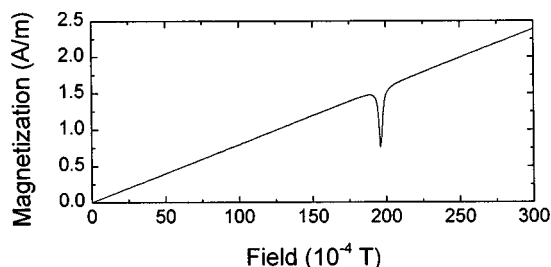


FIG. 1. Curve of M_z vs B_z given by Eq. (2). The dip in the otherwise linear curve occurs at the resonant field. In our MRFM experiments, we measure the second derivative of this curve to detect the nonlinear region near resonance.

^{a)}Electronic mail: moreland@boulder.nist.gov

$$M_z = \frac{\chi}{\mu} B \left\{ 1 - \frac{\gamma^2 \omega^2 B_{\text{eff}}^2 \tau^4}{[1 + (\gamma B_z - \omega)^2 \tau^2][1 + (\gamma B_z + \omega)^2 \tau^2] + \frac{1}{2} \gamma^2 B_{\text{eff}}^2 \tau^2 (1 + \omega^2 \tau^2 + \gamma^2 B_z^2 \tau^2)} \right\} \quad (2)$$

for the case of saturating rf fields. In Eq. (2) the spin–spin and spin–lattice relaxation times are equivalent, so $T_1 = T_2 = \tau$, as is the case for the ESR sample used in our experiments. Here χ and μ are the magnetic susceptibility and permeability of the resonant field sensor, γ is the gyromagnetic ratio for the spins under resonance, and B_z is a quasi-static background magnetic field.

Equation (2) may be used to predict M_z for an ESR experiment as shown in Fig. 1. A dip occurs in the magnetization as a function of B_z , and hence the force measured by the cantilever, when B_z matches the resonance condition $B_z = \omega/\gamma$. Because the resulting force of the resonant term [the second term of Eq. (2)] can be small relative to the linear, paramagnetic, background term, ac detection is used to measure the nonlinear resonant term proportional to $\partial^2 M_z / \partial B_z^2$. This is accomplished by modulating the background applied field at a frequency ω_m such that

$$B_z = B_0 + B_m \sin(\omega_m t). \quad (3)$$

Both the linear and nonlinear terms of Eq. (2) produce a time-varying magnetization at ω_m near resonance. The nonlinear term also produces higher frequency magnetization components at higher harmonics. In particular, the $2\omega_m$ component of M_z is proportional to the second derivative of Eq. (2).¹¹ By expanding Eq. (1) in a Taylor series about $B_z = B_0$, we find the second harmonic force component is

$$F_z^{(2)} = V \frac{B_m^2}{4} \left(\frac{\partial^2 M_z}{\partial B_z^2} \right) \bigg|_{B_z=B_0} \frac{\partial B_z}{\partial z}, \quad (4)$$

where the $2\omega_m$ component of M_z is given by $M^{(2)} = (B_m^2/4)(\partial^2 M_z / \partial B_z^2)$. If, in addition, ω_m is set to exactly half of the cantilever’s resonant frequency, the sensitivity to $F_z^{(2)}$ will be increased by a factor proportional to the mechanical Q of the cantilever. Experimentally, we have measured Q values as high as 10^4 when operating in vacuum to minimize air damping.

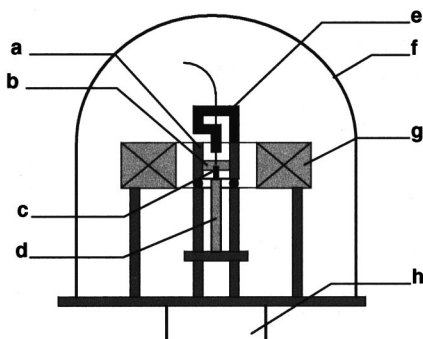


FIG. 2. Schematic of MRFM system: (a) MRFM head (see Fig. 3 for details), (b) kinematic mount, (c) permanent magnet, (d) piezoelectric tube scanner, (e) fiber optic positioner, (f) bell jar, (g) background field electromagnet, (h) port to vacuum pump.

Figure 2 shows a schematic of our entire MRFM system, and Fig. 3 reveals the details of our MRFM head. A small ($<10 \mu\text{m}$) particle of 2,2-diphenyl-1-picrylhydrazyl hydrate (DPPH, an organic compound with 95% free radicals) is mounted on a commercially available cantilever micromachined single crystal silicon with nominal dimensions of $440 \mu\text{m}$ length, $40 \mu\text{m}$ width, and $2 \mu\text{m}$ thickness. This results in a spring constant on the order of 0.1 N/m and a resonant frequency of 15 kHz . The cantilever motion is measured with a fiber optic interferometer.¹² A SmCo magnet 1.5 mm in diameter and 7.1 mm long provides a field gradient and also contributes to the local background field B_z . The magnet is mounted on a piezoelectric scanner, enabling us to scan the magnet relative to the DPPH sensor over an area of $150 \mu\text{m} \times 150 \mu\text{m}$. This large scanning range is unique to our instrument and will be useful for imaging magnetic structures like recording heads.

DPPH particles are mounted on a cantilever with the aid of atomic force microscope (AFM) with a large sample stage and an integrated optical microscope. Small amounts of vacuum grease and DPPH are placed on separate areas of a glass slide. The cantilever is then brought into contact first with the grease, which we use to adhere the DPPH to the cantilever,¹³ and then with the desired DPPH particle using the precise positioning of the AFM. Particles as small as a few micrometers may be easily mounted onto the end of a cantilever with this method. To improve the particle geometry, the DPPH particle can be heated to its melting point after adhesion to the cantilever,¹⁴ at which time it coalesces into a small hemispherical pancake. The size of the pancake can be controlled by carefully monitoring the subsequent evaporation of the DPPH under a high power microscope. This mounting procedure is a key element to MRFM field mapping experiments. Submicrometer imaging will require

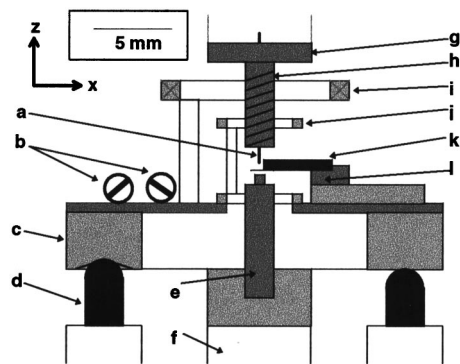


FIG. 3. Schematic of our MRFM head: (a) fiber to detect cantilever motion; (b) rf tuning capacitors; (c) kinematic mount; (d) ball bearing index; (e) SmCo permanent magnet; (f) piezoelectric tube scanner; (g) fiber positioning stage; (h) temperature compensated fiber chuck; (i) background field modulation coils; (j) modified Aldermann–Grant rf resonator; (k) cantilever chip; (l) piezoelectric stack.

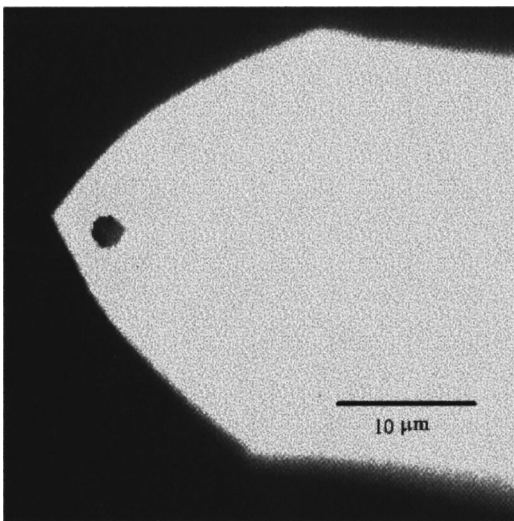


FIG. 4. Optical micrograph of a $3\ \mu\text{m}$ DPPH particle (black dot) mounted near the end of a cantilever.

even smaller particles with uniform shapes. Figure 4 shows a representative DPPH particle (black dot) mounted on the end of a cantilever.

A modified Aldermann–Grant resonant coil geometry serves as the source for the transverse field B_{rf} .¹⁵ This geometry was developed for conventional MRI microscopy and is useful in MRFM because it allows easy access to the interior of the coil from the top and bottom, as well as from the sides. When combined with a 22 pF series and a 3 pF parallel capacitor, our coil has a resonant frequency of 550 MHz and a Q of 10 (see Fig. 5). To verify the presence of rf power inside the resonant coil, the applied rf power was increased until the DPPH sample melted. Actual MRFM experiments were then carried out at a sufficiently low rf power to avoid melting the DPPH.

The melting experiment described above demonstrates that the intense electric field within the modified Aldermann–Grant coil serves as a heat source in addition to the field modulation coil and the electromagnet used generates the background field. The resulting temperature gradi-

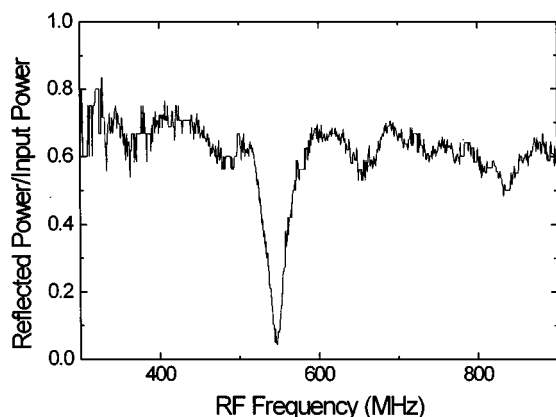


FIG. 5. rf spectrum of our modified Aldermann–Grant coil. A resonance frequency of 550 MHz and a Q of 10 are obtained with a 22 pF series and a 3 pF parallel capacitor.

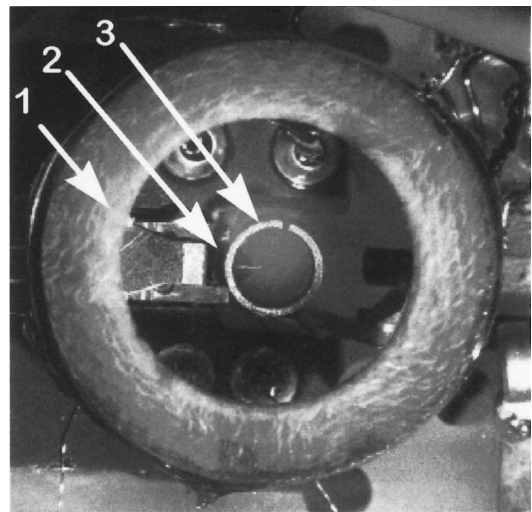


FIG. 6. Top-view photograph of MRFM head, showing (1) modulation coil, (2) cantilever chip, and (3) modified Aldermann–Grant coil. The permanent magnet is radially centered in the rf coil from below, and an optical fiber approaches the cantilever from the top.

ents result in thermal drift between the optical fiber and the cantilever, thus changing the sensitivity of the interferometer as the system drifts through a fringe. To compensate for this drift, the brass fiber chuck is heated to a few degrees above ambient with a small bifilar heating coil, causing the chuck to expand. The length of the chuck is controlled with a feedback system that maintains a constant average fiber–tip separation by monitoring the intensity of the interference fringe and then changing the heater current to maintain a constant dc output voltage from the interferometer near the center of a fringe. No more than 50 mW are typically required to maintain a constant fiber–tip spacing. Note that the time constant of this system is on the order of several seconds, so it is not affected by motion of the cantilever near its resonant frequency. The temperature compensated fiber chuck makes it possible to position the fiber with a standard five-axis positioning stage. Because the system can accommodate several fringes of motion, we have the dynamic range necessary to cancel thermal effects *in situ*, while taking data. This eliminates waiting for long periods for the system to thermalize before data can be taken.

The entire microscope head is placed inside an electromagnet that provides an additional B_z as large as ± 100 mT. A small modulation coil provides a background field modulation in the z direction of up to 0.5 mT (5 G) rms. The head of our microscope is specifically designed to interface mechanically and electrically to a commercial scanning probe microscope system, enabling us to leverage existing electronic feedback and piezoelectric scanning systems. The microscope is operated in a moderate vacuum with a pressure of 1.3×10^{-3} Pa (10^{-5} Torr) to eliminate air damping of the cantilever, which increases the Q of the cantilever. Figure 6 is a top-view photograph of the microscope's head. The fiber and gradient magnet are not shown in the photograph.

A high Q cantilever is required for maximum force sensitivity, but the long response time and extremely narrow bandwidth of such systems are impractical for most imaging

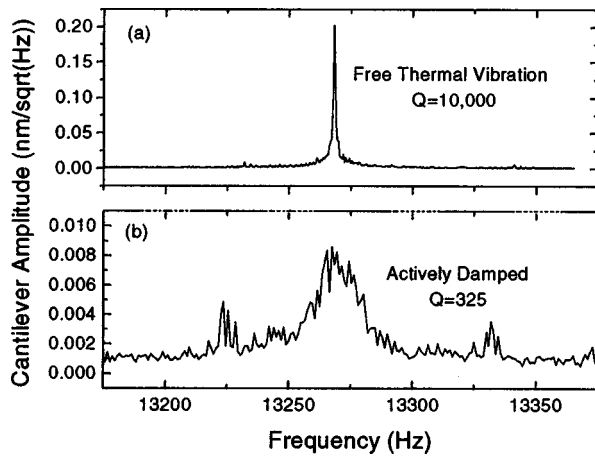


FIG. 7. Cantilever thermal vibration: (a) undamped in vacuum, (b) actively damped.

applications. Image acquisition times of several days are required for free ringing mechanical detectors of this type. Active damping of the cantilever vibration allows us to minimize the thermal excitation of the cantilever, reduce the response time of the system, and increase the effective detection bandwidth while maintaining an acceptable SNR.⁷ Our system has a piezoelectric cantilever mount that is used to apply the counter force necessary for active damping.

III. INSTRUMENT SENSITIVITY

Mapping field contours with high resolution requires a small resonant sample, which unfortunately reduces the number of spins in the sensor and hence the force on the cantilever. The predominant noise source for our instrument is the thermal excitation (Brownian motion) of the cantilever. Consider the cantilever as a classical damped harmonic oscillator subject to thermal noise. For a cantilever with spring constant k , resonant frequency f_0 , and mechanical quality factor Q operating at a temperature T with a measurement bandwidth Δf , the minimum detectable force is¹⁶

$$F_{\min} = \left(\frac{2k\Delta f k_B T}{\pi Q f_0} \right)^{1/2}. \quad (5)$$

Figure 7(a) shows a typical vibration spectrum of a thermal-noise limited cantilever. Given the spring constant of 0.1 N/m and the experimentally measured resonant frequency of 13.268 kHz and Q of 10 000, Eq. (5) yields a theoretical thermal noise force of 1.4×10^{-15} N/ $\sqrt{\text{Hz}}$ rms at a temperature of 300 K. Our measured noise is $F_{\text{meas}} = kz/Q = 2.0 \times 10^{-15}$ N/ $\sqrt{\text{Hz}}$ rms, indicating that our system is operating near the thermal noise limit. We determine our experimental spin sensitivity $F_z^{(2)}$ based on Eq. (4) given our instrumental parameters of $B_m = 0.4$ mT(4 G), $\omega = 2\pi \times 550$ MHz, and $\partial B/\partial z = 100$ T/m, and given the reported spin density¹¹ for DPPH of 2.3×10^{21} cm⁻³, we find a single spin force of $F_{\text{spin}} = 1.6 \times 10^{-25}$ N. Thus, at the estimated field gradient of 100 T/m (1 G/ μm), we have an electron spin sensitivity of 1.25×10^{10} Hz^{-1/2}. This means we can detect magnetic resonance in a DPPH sample of radius 1 μm with a SNR of 1 in a 1 Hz bandwidth.

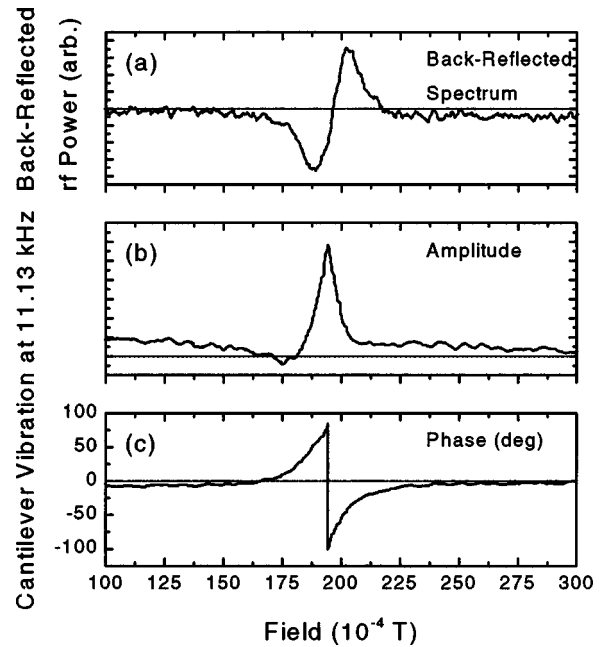


FIG. 8. Single-shot ESR spectra: (a) back-reflected wave spectrum showing the reflected rf power as a function of the applied magnetic field for a 1 mm³ sample; (b) MRFM spectrum showing the cantilever's amplitude of vibration, which peaks at resonance; (c) the cantilever phase corresponding to (b). For (b) and (c), a 15 μm diam sample was used. In all three cases the field was swept at 2.5×10^{-4} T/s(2.5 G/s), and a lock-in time constant of 200 ms was used. The rf frequency was 544.2 MHz, corresponding to the observed resonant field of 194.2×10^{-4} T.

As discussed above, active damping is employed to minimize the thermal oscillations of the cantilever. The effectiveness of active damping is demonstrated in Fig. 7. Figure 7(a) shows the free cantilever oscillation at 1.3×10^{-3} Pa(10^{-5} Torr), and 7(b) shows the cantilever oscillation when the active damping signal is applied by the piezoelectric mount. The cantilever vibration is reduced by a factor of 30.

The three critical components of any MRFM microscope are the rf resonator, the modulation field coil, and the gradient magnet. The functionality of the combination of these components was tested by performing conventional rf reflected wave experiments. In these experiments a macroscopic 1 mm³ DPPH sample replaces the optic fiber/cantilever assembly in the rf coil. A modulation field of a few amperes per meter was added to the background field. When the magnitude of the swept background field satisfied the resonant condition, the absorption of rf power by the DPPH changed the impedance of the rf coil. We measured the modulation of the back-reflected rf wave with a lock-in amplifier. Figure 8(a) shows a typical ESR spectrum showing the expected derivative line shape of the rf absorption as a function of sweep field.

IV. RESULTS AND DISCUSSION

The amplitude and phase of a single shot ESR spectrum measured using mechanical detection of the second harmonic component of the force is shown in Figs. 8(b) and 8(c). The spectra of Fig. 8 illustrate the primary advantage of MRFM

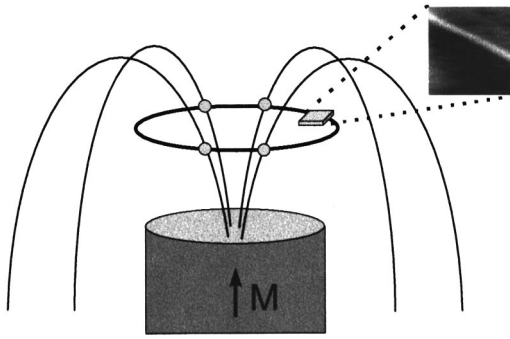


FIG. 9. Mapping of a field contour. The permanent gradient magnet produces field lines in space. Contours of constant field, represented by the dark ring, can be found at any height above the magnet. The DPPH resonant sensor is raster scanned over a small portion of the magnet. This area is depicted as the small square. The constant field contour shows up in the MRFM image as a bright line. See Fig. 10.

over other techniques used for high resolution field mapping: the magnitude of the signal does not need to be calibrated. Only the position (in either background field or rf frequency) of the resonance is important.

A comparison between the back-reflected wave spectrum of Fig. 8(a) and the MRFM spectra of Figs. 8(b) and 8(c) shows that our MRFM system delivers the same or better SNR with a micrometer sample than the back-reflected spectrum using a millimeter sample. This is explained by the fact that our system is not optimized for back-reflected wave spectroscopy. We recognize that state-of-the-art ESR spectrometers are capable of measuring the spectrum of DPPH particles only a few micrometers in size with good SNR. With MRFM, however, it should be possible to measure sub-micrometer samples and also to image these small samples in three dimensions or use the small resonant sample as a field probe as is the case being discussed here.

We use the following procedure to produce a high resolution field contour map at a height of 1.5 mm above the permanent magnet: First, the cantilever with the DPPH field probe is positioned above the permanent magnet using the kinematic stage of the microscope. We then determine the resonance field by sweeping the background field to find the resonance peak. The background field is then kept fixed at this value. Finally the permanent magnet is raster scanned with a piezoelectric tube in x and y below the DPPH field probe mounted on the cantilever. The cantilever amplitude or phase of vibration is recorded as a function of permanent magnet position. Figure 9 describes this step schematically. Although the field contours directly above the center of a cylindrical magnet are circular, the resulting contour should appear as a line if only a small portion of that circle is imaged.

The resulting field contour map appears as shown in Fig. 10. The black-to-white contrast in the figure represents low-to-high vibration amplitude of the cantilever. The white areas of large amplitude are where the resonance condition $B_z = B_{\text{applied}} + B_{\text{magnet}} = \omega/\gamma$ is met. Given that $\gamma = 1.76 \times 10^{11} \text{ s}^{-1} \text{ T}^{-1}$ for DPPH, $\omega = 2\pi \times 550 \text{ MHz}$ and $B_{\text{applied}} = -36 \text{ mT}$, we find that $B_{\text{magnet}} = +16.4 \text{ mT}$ along the white line in Fig. 10. The cross-sectional line scan reveals a full-

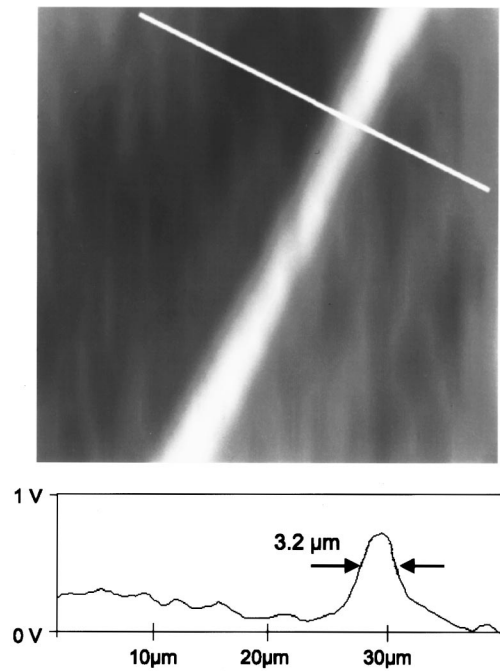


FIG. 10. Field contour map. This is a map of the cantilever vibration amplitude as measured 1.5 mm above a permanent magnet. The white areas correspond to regions in which the resonance condition is met, and $B_{\text{magnet}} = 16.4 \text{ mT}$. The cross-sectional scan reveals a spatial resolution of $3.2 \mu\text{m}$ obtained with a $7 \mu\text{m}$ diam DPPH field probe. A 200 ms time constant and 0.2 Hz scan rate was used to capture this $40 \mu\text{m} \times 40 \mu\text{m}$ image.

width-at-half-maximum (FWHM) spatial resolution of $3.2 \mu\text{m}$ obtained with a $7 \mu\text{m}$ diameter DPPH field probe.

Each line scan in the image of in Fig. 10 represents a magnetic resonance spectrum. We are sweeping the local field by physically moving the DPPH particle. The magnetic linewidth of the MRFM resonance δB_{MRFM} is related to local field gradient $\partial B/\partial x$, the particle diameter d , the intrinsic spectral linewidth of DPPH δB_{spec} , and the modulation field δB_{mod} . The corresponding spatial linewidth of the MRFM resonance is $\delta B_{\text{MRFM}} \cdot (\partial B/\partial x)^{-1}$. $\delta B_{\text{MRFM}} \approx \delta B_{\text{PART}} + \delta B_{\text{INSTR}}$, where $\delta B_{\text{PART}} \approx d/3 \cdot \partial B/\partial x$ is the approximate ‘‘magnetic size’’ of a spherical particle and $\delta B_{\text{INSTR}} = (\langle \delta B_{\text{spec}} \rangle^2 + \langle \delta B_{\text{mod}} \rangle^2)^{1/2}$ is the predicted instrumental spectral resolution. We try to set $\delta B_{\text{PART}} \approx \delta B_{\text{INSTR}}$ for maximum SNR. Given the experimental conditions for the $7 \mu\text{m}$ DPPH particle described above we estimate $\delta B_{\text{MRFM}} \approx 0.5 \text{ mT}$ (5 G) and $\delta B_{\text{MRFM}} \cdot (\partial B/\partial x)^{-1} \approx 8 \mu\text{m}$. These values are somewhat larger than our experimental observations of 0.19 mT (1.9 G) and $3.2 \mu\text{m}$, respectively. Given the uncertainties regarding both the shape of the particle (the spherical approximation may not apply) and the magnitude of the modulation field near the particle (the field may be reduced by eddy currents in the gradient magnet) we feel that the measured linewidths are within reasonable limits.

We also note that particle translation rate, $\Delta x/\Delta t$, must be slow compared to the instrument response time. The local field must change slower than the time necessary for the cantilever oscillation amplitude to equilibrate $-t > Q/f_0$. Active damping effectively reduces Q so that Q/f_0 is a few milliseconds and thus much lower than the typical lock-in

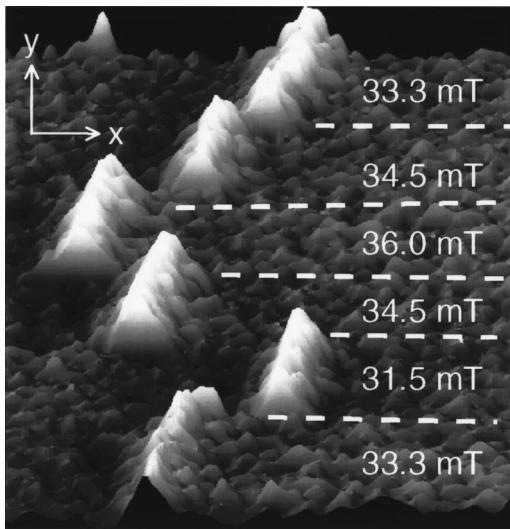


FIG. 11. Field contour map similar to Fig. 8, but with a changing background field. Values of the changing applied field are marked on the image. This map allows us to determine the local field gradients $\partial B_{\text{magnet},z}/\partial x \approx 56 \text{ T/m}$ and $\partial B_{\text{magnet},z}/\partial y \approx 20 \text{ T/m}$, giving a resultant lateral field gradient of 59 T/m ($0.59 \text{ G}/\mu\text{m}$). A $15 \mu\text{m}$ diam field probe was used to obtain this image. A 500 ms time constant, and 0.1 Hz scan rate was used to capture this $150 \mu\text{m} \times 150 \mu\text{m}$ image.

amplifier time constant t of 200 ms for the data reported here. In addition, $\Delta x/\Delta t$ must be slow enough so δB_{INSTR} is scanned in a time period greater than t . In other words $\delta B_{\text{INSTR}} > t \cdot (\partial B/\partial x) \cdot (\Delta x/\Delta t)$ which is also true for the experiments reported here.

We can adjust the applied magnetic field to find a different contour line of the magnet. In Fig. 11 we show a contour line similar to that in Fig. 10. However, instead of maintaining a constant applied magnetic field, we changed B_{applied} during the scan as indicated by the dashed lines. The white parts of the image still correspond to positions where the resonance condition is met. By changing the applied field we can measure $\partial B_{\text{magnet},z}/\partial x \approx 56 \text{ T/m}$ and $\partial B_{\text{magnet},z}/\partial y \approx 20 \text{ T/m}$, with the resultant lateral field gradient of 59 T/m ($0.59 \text{ G}/\mu\text{m}$). At higher applied fields the bright areas of the image show the regions of lower B_{magnet} , and vice versa. The images in Figs. 10 and 11 were taken over roughly the same area. If we assume approximately the same field gradients in both cases, we can estimate our field resolution to be the field gradient times the FWHM spatial resolution. Using the gradient of 59 T/m from Fig. 11 and the linewidth of $3.2 \mu\text{m}$ from Fig. 10, for which we used a much smaller resonant probe, we find a field resolution of 0.19 mT (1.9 G).

The spatial resolution in Fig. 11 is lower than that of Fig. 10 because a $15 \mu\text{m}$ diam probe was used, rather than the smaller probe used to acquire Fig. 10. Both spatial and field resolution are determined not only by the particle size, but also the local field gradient and the ESR linewidth. The spatial resolution of the system is limited by the larger of either the particle size, or the ESR linewidth divided by the field gradient. Similarly, field resolution is limited by the larger of either the ESR linewidth or the product of the local field gradient and the particle size. Alternative peak-detection algorithms, such as taking the derivative or measuring the phase

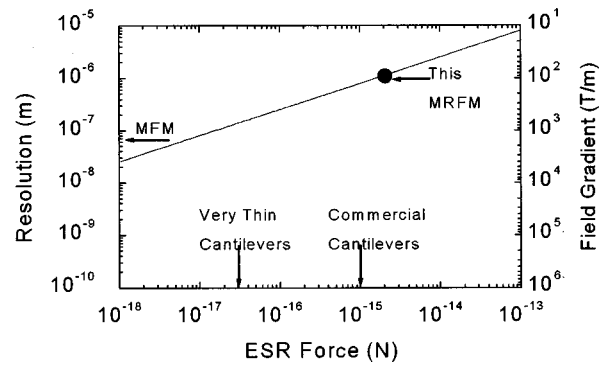


FIG. 12. Resolution of MRFM as a function of ESR force. In this plot, resolution is given by the size of the resonant field probe. The field gradient dB_z/dz was adjusted so that the product of the natural ESR linewidth and $(dB_z/dz)^{-1}$ was equivalent to the size of the field probe. Force sensitivities attainable at room temperature with conventional and customized ultra thin cantilevers (see Ref. 6) are marked for reference, as is the spatial resolution of MFM.

of the resonance peak, may be used to improve the resolution. In particular, we propose using the zero crossing of the phase as a resonance field criterion. As shown in Fig. 8(c), the very sharp zero crossing may eliminate many of the ambiguities that can occur when trying to determine the location of the resonance curve. One important result from these relationships is that, in regions of high field gradient, the spatial resolution of MRFM improves until the particle size limit is reached. The images of Figs. 10 and 11 demonstrate that we are in the particle size limit.

V. OUTLOOK AND CONCLUSION

The potential for MRFM as a calibrated, room temperature, high resolution magnetic field probe is shown in Fig. 12. Spatial resolution of 100 nm , comparable to MFM, and field resolution on the order of 0.1 mT (1 Oe) are possible at room temperature with a small enough resonant field probe, field gradients of 1000 T/m ($10 \text{ Oe}/\mu\text{m}$), and custom manufactured ultrathin cantilevers. This resolution is sufficient to characterize magnetic read and write heads which have typical magnetic pole lengths on the order of $1 \mu\text{m}$ and gap spacing of $100\text{--}200 \text{ nm}$. The required field gradients should be relatively easy to obtain when fields are mapped close to the magnetic head. As noted earlier, any reduction in spatial resolution due to a lower field gradient is of little concern, because reduced field gradients indicate a lack of spatial resolution field artifacts that would require high resolution imaging.

With 100 nm spatial resolution and 0.1 mT (1 G) field resolution, the MRFM can fill an important gap in the technology of magnetic field mapping, as shown in Table I. Magnetic force microscopy (MFM) is the technique most widely used today because of its high spatial resolution and ease of use. Unfortunately, calibrated MFM field measurements require precise knowledge of the geometrical shape and magnetic properties of the magnetic coating on the tip. Both Hall probes and SQUID magnetometers suffer from the requirement of cryogenic temperatures. Although Lorentz microscopy and electron holography can provide field maps with

TABLE I. Comparison of common magnetic field mapping techniques.

Technique	Spatial resolution (μm)	Field resolution 10^{-4} T	Quantitative
MFM ^a	0.050	1	no
SQUID ^b	1	0.1	yes
Hall probe ^c	0.85	0.001	yes
ac microloop ^d	2	0.1	yes
MR ^e	0.1×1	0.1	yes
Electron holography ^f	0.003	0.1	yes
Lorentz microscopy ^g			
Current MRFM	3.2	0.64	yes
Future MRFM	0.05	≤ 0.1	yes

^aReference 18.^bReference 19.^cReference 20.^dReference 21.^eReference 22.^fReference 23.^gReference 24.

10^{-5} T field and 2 nm spatial resolutions, ultrahigh vacuum operation and calculation intensive image reconstruction limit their use.

For MRFM field mapping, the real challenge lies in the force detection of magnetic resonance from a probe with a 100 nm diameter—a volume 1000 times smaller than the ESR probe used in this article. This requires improving our SNR by a factor of 30 in order to perform imaging at just the one-standard-deviation level. Operating in a region of higher field gradient along the z axis will increase the measurable force from each spin proportionately and is the only way to improve spin sensitivity without using softer cantilevers or resorting to cryogenic temperatures. Ultrathin cantilevers (60 nm thick) with attonewton sensitivities have already been demonstrated.⁵ We are building a micromachining facility to produce our own ultrasensitive cantilevers and this effort will make it possible for us to improve force sensitivity required to reduce the resonance probe volume by several orders of magnitude. Reduced thermal noise at cryogenic temperatures would accomplish two things. First, the Brownian motion of the cantilever is reduced in accordance with Eq. (5). Second, at 1.2 K, the susceptibility of DPPH is increased by a factor of 100,¹⁷ resulting in a $100\times$ increase in the force experienced by a cold ESR field probe over an identical probe operating at room temperature.

The range of fields measurable using our MRFM apparatus can be extended by using a broadband microwave field source, such as a strip line. In this way, we may perform swept-frequency rather than swept-field ESR measurements. We can then rely on the magnetic device under test to provide both the background field B_z and the field gradient. Large external B_z fields, which could alter the device under test, will no longer be required.

In summary, we have demonstrated a MRFM for use in high-resolution quantitative magnetic field mapping. The force detection system has enabled us to achieve a spatial

resolution of $3.2 \mu\text{m}$ and a field resolution of 1.9 mT (1.9 G) with a SNR of 30 limited by thermal noise. Improvements in overall sensitivity by operating in a higher field gradient with more sensitive cantilevers hold promise for 100 nm spatial resolution and 0.1 mT (1 G) field resolution at room temperature. Such an instrument could have applications for the quantitative characterization of magnetic structures including magnetic read/write heads and magnetic data bits.

ACKNOWLEDGMENTS

One of the authors, T.R., acknowledges support from the NRC Postdoctoral Research program, and ML has been supported by the Deutscher Akademischer Austauschdienst (DAAD): “Die Arbeit wurde mit Unterstützung eines Stipendiums im Rahmen des Gemeinsamen Hochschulsonderprogramms III von Bund und Ländern über den DAAD ermöglicht.” The authors acknowledge Dan Rugar, John Sidles, Chris Hammel, and Gareth Eaton for helpful discussions and insight.

¹J. A. Sidles, Appl. Phys. Lett. **58**, 2854 (1991).²D. Rugar, C. S. Yannoni, and J. A. Sidles, Nature (London) **360**, 563 (1992).³O. Züger, S. T. Hoen, C. S. Yannoni, and D. Rugar, J. Appl. Phys. **79**, 1881 (1996).⁴A. Schaff and W. S. Veeman, Appl. Phys. Lett. **70**, 2598 (1997).⁵Z. Zhang, P. C. Hammel, and P. E. Wigen, Appl. Phys. Lett. **68**, 2005 (1996).⁶T. D. Stowe, K. Yasumura, T. W. Kenny, D. Botkin, K. Wago, and D. Rugar, Appl. Phys. Lett. **71**, 288 (1997).⁷T. R. Albrecht, P. Grütter, D. Horne, and D. Rugar, J. Appl. Phys. **69**, 668 (1991); J. L. Garbini, K. J. Bruland, W. M. Dougherty, and J. A. Sidles, *ibid.* **80**, 1951 (1996); K. J. Bruland, J. L. Garbini, W. M. Dougherty, and J. A. Sidles, *ibid.* **80**, 1959 (1996).⁸K. Wago, O. Züger, R. Kendrick, C. S. Yannoni, and D. Rugar, J. Vac. Sci. Technol. B **14**, 1197 (1996).⁹K. Wago, O. Züger, J. Wegener, R. Kendrick, C. S. Yannoni, and D. Rugar, Rev. Sci. Instrum. **68**, 1823 (1997).¹⁰M. A. Garstens and J. I. Kaplan, Phys. Rev. **99**, 459 (1955).¹¹O. Züger and D. Rugar, J. Appl. Phys. **75**, 6211 (1994).¹²D. Rugar, H. J. Mamin, and P. Guethner, Appl. Phys. Lett. **55**, 2588 (1989).¹³We have found that the solvents of many traditional adhesives dissolve or otherwise chemically react with DPPH. We use Dow Corning high vacuum silicone grease which does not react with DPPH. Trade names are used to accurately specify the experimental procedure, and do not imply endorsement by NIST. Similar products by other manufacturers may work as well or better.¹⁴E. J. Hill and J. H. Burgess, Thin Solid Films **11**, 99 (1972).¹⁵Z. Zhang, P. C. Hammel, and G. J. Moore, Rev. Sci. Instrum. **67**, 3307 (1996).¹⁶J. A. Sidles and D. Rugar, Phys. Rev. Lett. **70**, 3506 (1993).¹⁷A. Van Itterbeek and M. Labro, Physica (Amsterdam) **30**, 157 (1964).¹⁸P. C. D. Hobbs, D. W. Abraham, and H. K. Wickramasinghe, Appl. Phys. Lett. **55**, 2357 (1989).¹⁹J. Dechert, K. Krischker, T. Göddenhenrich, M. Mück, and C. Heiden, IEEE Trans. Appl. Supercond. **7**, 3143 (1997).²⁰A. Oral, S. J. Bending, and M. Henini, J. Vac. Sci. Technol. B **14**, 1202 (1996).²¹R. S. Indeck, M. J. Vos, E. G. Persson, N. Curland, and J. H. Judy, IEEE Trans. Magn. **23**, 2491 (1987).²²S. Y. Yamamoto and S. Schultz, J. Appl. Phys. **81**, 4696 (1997).²³A. Tonomura, Rev. Mod. Phys. **59**, 639 (1987).²⁴K. Tsuno, Rev. Solid State Sci. **2**, 623 (1988).